Fluid drainage in erodible porous media

Joanna Schneider,[1] Christopher A. Browne,[1] Malcolm Slutzky,[2] Cecilia A. Quirk,[3] Daniel B. Amchin,[1] and Sujit S. Datta[1,*]

[1]*Department of Chemical and Biological Engineering, Princeton University, Princeton, New Jersey 08544, USA*
[2]*Department of Physics, Princeton University, Princeton, New Jersey 08544, USA*
[3]*Department of Operations Research and Financial Engineering, Princeton University, Princeton, New Jersey 08544, USA*

(Received 2 March 2023; revised 10 July 2023; accepted 14 September 2023; published 5 October 2023)

Drainage, in which a nonwetting fluid displaces a wetting fluid from a porous medium, is well studied for media with unchanging solid surfaces. However, many media can be eroded by drainage, with eroded material redeposited in pores downstream, altering further flow. Here we use theory and simulation to examine how these coupled processes both alter the overall fluid displacement pathway and help reshape the solid medium. We find two drainage behaviors with markedly different characteristics and quantitatively delineate the conditions under which they arise. Our results thereby help expand the current understanding of these rich physics, with implications for applications of drainage in industry and the environment.

DOI: 10.1103/PhysRevResearch.5.043015

I. INTRODUCTION

Drainage is the process by which a nonwetting fluid displaces a wetting fluid from a porous medium. It underlies a broad range of environmental and industrial processes, including groundwater contamination, oil migration and recovery, gas venting from sediments, CO_2 sequestration, soil drying, and the operation of porous membranes [1–17]. Therefore, extensive research has sought to develop ways to predict the displacement pathway taken by the nonwetting fluid [18,19], building on the seminal model of invasion percolation proposed by Wilkinson and Willemsen four decades ago [20].

In this model, the medium is assumed to be composed of a static solid matrix of uniform wettability (with a prescribed three-phase contact angle θ) that houses an interconnected network of pores with randomly varying sizes. The nonwetting fluid is taken to be much more viscous than the wetting fluid, and its flow is considered to be very slow; in this limit, which characterizes many real-world processes, capillary forces at the immiscible fluid interface dictate the resulting displacement pathway as detailed further in Appendix A. In particular, the nonwetting fluid cannot invade a pore of entrance radius r until the capillary pressure difference across the interface reaches a threshold $\Delta p_c \equiv 2\gamma \cos\theta / r$, where γ is the interfacial tension between the two fluids. Hence, the fluid displacement proceeds one pore at a time, with the nonwetting fluid invading the largest pore accessible to it and therefore the lowest capillary pressure threshold successively. The fluid displacement pathway is then determined by random local variations in pore size, resulting in a characteristic ramified and disordered displacement pattern known as capillary fingering (CF) [18,21–34].

While this foundational model has been validated in highly controlled laboratory studies, it makes a strong assumption that often does not hold in practice—that the structure of the solid matrix is unchanging. In reality, capillary forces at the immiscible fluid interface can restructure the matrix as detailed further in Appendix B. One way this can happen is by deforming or fracturing the overall medium [35,36]. Another way is by eroding frangible [37] and plastocapillary [38] material from the walls of the solid matrix and redepositing it within the pore space downstream. A prominent example is the layers of colloidal particles, inorganic precipitates, and organic matter that frequently coat the mineral grains making up soils, sediments, and subsurface aquifers/reservoirs [39–49]. Field observations indicate that fluid drainage caused by processes like wetting/drying cycles and contaminant/oil migration can erode and redeposit these materials, impacting subsequent transport over large scales [50–54]. However, despite their common occurrence, studies of the influence of solid erosion and deposition on fluid drainage in porous media (and vice versa) are lacking.

Here we incorporate these physics into the classic framework of invasion percolation. Our numerical simulations reveal two drainage behaviors whose fluid displacement and solid deposition patterns differ dramatically from standard CF: rapid clogging (RC), in which redeposited material rapidly clogs the pore space and arrests subsequent flow, and erosion-enhanced fingering (EEF), in which constriction of some pores by deposition unexpectedly enables the nonwetting fluid to invade a greater fraction of the medium. Furthermore, we use calculations to delineate the conditions under which these different behaviors arise,

*ssdatta@princeton.edu

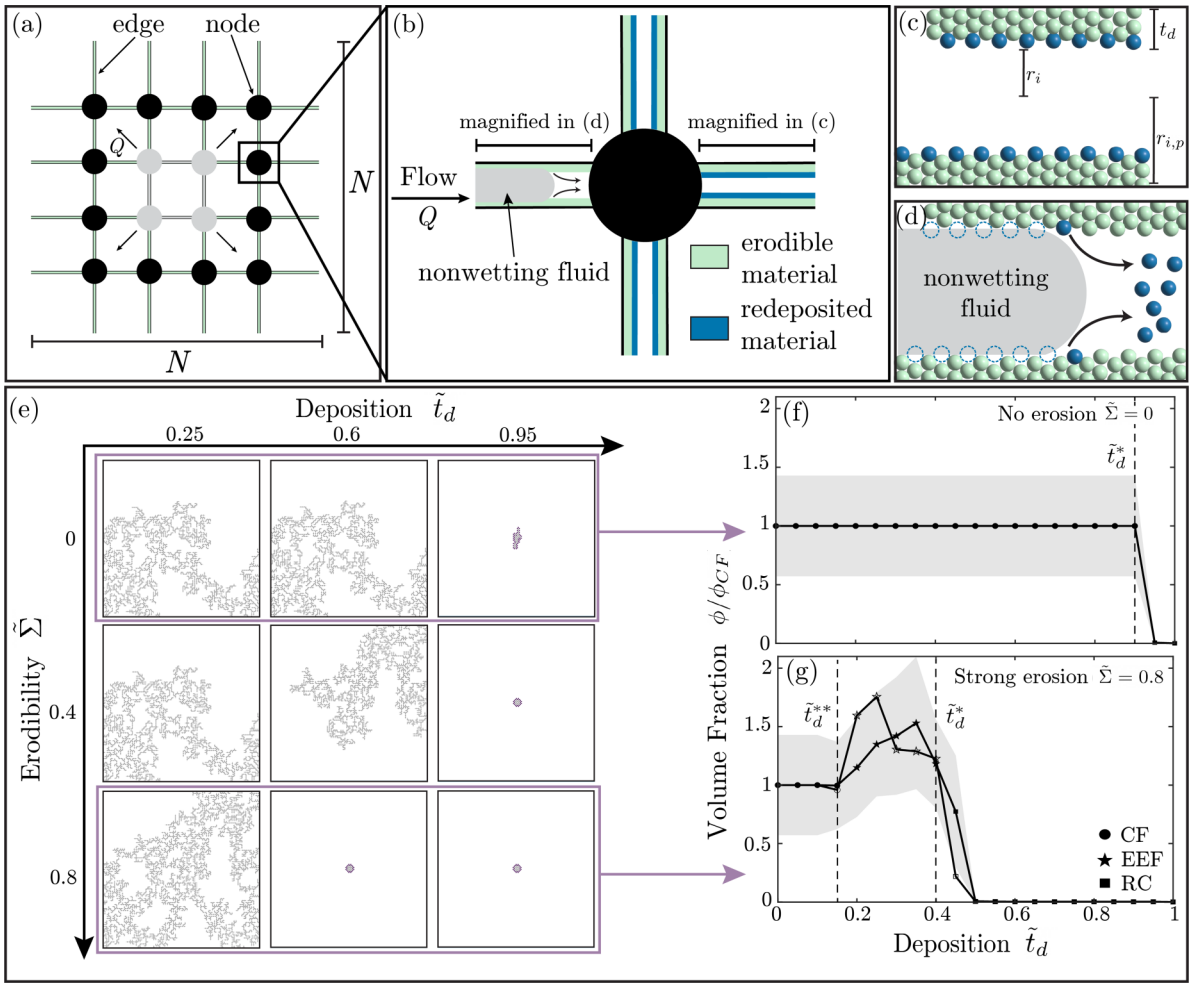

FIG. 1. Network modeling of fluid drainage in an erodible porous medium reveals different drainage behaviors. (a) Schematic of the 2D network model, with $N \times N$ nodes representing the pore bodies and the edges representing the interconnecting pore throats. (b) Magnified view of a single-pore body. (c) Pore throats initially have a pristine radius $r_{i,p}$, with an initial layer (mint) of erodible material t_d thick. (d) As the nonwetting fluid enters a pore during drainage, it erodes some of this material, redepositing it into connected throats (blue). Numerical simulations reveal different drainage behaviors arising from solid erosion and deposition, as represented in the state diagram in (e) showing magnified views of the final drainage patterns across a wide range of $\tilde{t}_d$ and $\tilde{\Sigma}$. Circular gray and purple markers indicate invaded and clogged pore throats, respectively, while gray pluses denote invaded pore bodies. We characterize these behaviors in (f) and (g) using the volume fraction of the pore space filled by the nonwetting fluid after drainage completes, ϕ, normalized by the case of standard capillary fingering ϕ_{CF}. Open symbols show the results for the single network used to generate the simulations shown in (e). Closed symbols and gray shading show the average and standard deviation, respectively, of results obtained over 100 different, but statistically identical, networks. (f) Without erosion ($\tilde{\Sigma} = 0$), drainage proceeds by CF [magnified view in (e)] until $\tilde{t}_d > \tilde{t}_d^* \approx 0.9$, above which the medium starts with so much erodible material that pores near the inlet are clogged. The medium transitions to rapid clogging, as shown by the top right image of (e). (g) With strong erosion ($\tilde{\Sigma} = 0.8$), drainage proceeds by CF only until $\tilde{t}_d > \tilde{t}_d^{**} \approx 0.15$, above which the nonwetting fluid unexpectedly explores more of the pore space than in CF. Drainage proceeds by erosion-enhanced fingering, as shown in the bottom left image of (e). With increasing $\tilde{t}_d > \tilde{t}_d^* \approx 0.4$, clogging increasingly dominates and drainage transitions back to RC.

governed by two dimensionless parameters that quantify how much of, and how easily, the solid matrix can be eroded.

II. MODEL DEVELOPMENT

To begin to unravel the complex physics underlying this problem, we examine a simple, but illustrative, example. Following the typical approach of pore-network modeling [55–57], we consider fluid drainage at a constant volumetric flow rate Q in a two-dimensional (2D) network of $N \times N$ nodes, which represent the pore bodies, with locations defined by an adjacency matrix with network connectivity c [Fig. 1(a)]. The edges between nodes are indexed serially by i and represent the constrictions (throats) between pores. Because p_c is locally maximum at these constrictions, they control both pore invasion and solid erosion. We thus focus our attention on the edges of the network; for simplicity, we assume that they compose the entirety of the pore space volume and approximate them as cylinders of uniform length L and pristine radii $r_{i,p}$ drawn randomly from a given distribution $\rho(r_{i,p})$.

To impart erodibility to this static matrix, we consider the inner wall of each pore throat to also be coated by a layer of erodible material prior to the initiation of drainage [47,58], initially of constant thickness t_d [Figs. 1(b) and 1(c)] distributed uniformly throughout the medium. The effective radius of throat i is then given by $r_i = r_{i,p} - t_d$, with a corresponding capillary pressure threshold $\Delta p_c(r_i) = 2\gamma \cos\theta / r_i$; here, we take $\theta = 0$. If $t_d \geqslant r_{i,p}$ for a given pore i, it is taken to start as clogged and is removed from the network. Guided by studies in single pores and on flat surfaces [38,59–67], we account for drainage-induced erosion using a simple rule: If a pore is invaded by the nonwetting fluid, the moving immiscible fluid interface erodes material from the wall [Fig. 1(d)] when $\Delta p_c(r_i)$ exceeds a threshold stress σ_y that quantifies the material's durability, analogous to a yield stress. For ease of notation, we indicate dimensionless quantities by tildes and nondimensionalize all length scales by $r_{p,\max} \equiv \max\{r_{i,p}\}$. The ratio $\tilde{\Sigma} \equiv \Delta p_c(r_{p,\max})/\sigma_y$ then compares the smallest capillary pressure that can possibly arise in the porous medium to the threshold erosion stress, that is, it describes the relative ease with which the immiscible fluid interface erodes material from the pore walls as it moves. We therefore call this dimensionless parameter the medium's erodibility.

Hence, as the nonwetting fluid invades a pore with throat radius r_i, the amount of material eroded from its walls depends on $\tilde{\Sigma}$. If $\tilde{\Sigma} < \tilde{r}_i$, erosion does not occur and the dimensions of the pore remain unchanged after drainage; the radius after the entire drainage process has completed, $\tilde{r}'_i$, remains equal to $\tilde{r}_i$. Above the threshold $\tilde{\Sigma} \geqslant \tilde{r}_i$, erosion causes the radius to increase to a new value $r'_i = 2\gamma/\sigma_y$, at which the corresponding capillary pressure becomes balanced by the threshold stress for erosion, or equivalently $\tilde{r}'_i = \tilde{\Sigma}$. However, there is a limit to how much material can be eroded from a pore: If the erodibility is so large that this new value $2\gamma/\sigma_y$ exceeds the pristine radius $r_{i,p}$ (that is, if $\tilde{\Sigma} > \tilde{r}_{i,p}$), then the pore throat radius saturates at its largest possible value $\tilde{r}'_i = \tilde{r}_{i,p}$. Given that we focus on the limit of capillary-dominated displacement of a low-viscosity wetting fluid, we neglect any possible coupling between solid erosion/deposition and viscous forcing (Appendix A); however, incorporating such additional complexities will be an important extension of our theoretical framework.

Finally, we also incorporate the subsequent deposition of the eroded material in the nondrained throats j directly connected to a drained eroded throat i. In particular, because we assume cylindrical pore throats with $N \gg 1$, we distribute the volume eroded from i proportionately to r_j^4, following mass conservation (detailed in Appendix C), reducing the values of $\tilde{r}'_j$ accordingly. However, if this process causes a pore throat j to become fully clogged, the excess volume of eroded material is returned to the parent i and the throat is removed from the network to prevent subsequent flow through it.

III. MODEL IMPLEMENTATION

To characterize the influence of solid erosion and deposition on fluid drainage, we perform numerical simulations of this model with $N = 200$, $c = 4$, and $\rho(\tilde{r}_{i,p})$ given by a uniform distribution spanning $\tilde{r}_{i,p} \in [0.83, 1]$; we find results similar to those described below when exploring other values of N, c, and forms of $\rho(\tilde{r}_{i,p})$, including those obtained from real-world media, as shown in Appendix D. For each simulation condition tested, parametrized by prescribed input values of $(\tilde{t}_d, \tilde{\Sigma})$, we run 100 unique iterations, each with $\tilde{r}_{i,p}$ randomly sampled from the same $\rho(\tilde{r}_{i,p})$. In each simulation, the pore bodies and throats all start saturated with the wetting fluid. We then initiate drainage by introducing the nonwetting fluid at the four central pore bodies. This choice of invasion starting from a central position is frequently made in pore network models [35,68]; however, we find similar results when drainage is initiated from one edge of the network instead (Appendix E), indicating that our findings hold more generally. During each time step, we then determine the connected component clusters of undrained pore bodies; the boundaries with these clusters delineate the invading nonwetting fluid interface or trapped wetting fluid regions. Following standard invasion percolation, we then identify the largest pore throat i, with the smallest capillary pressure threshold $\Delta p_c \sim 1/\tilde{r}_i$, along the invading nonwetting fluid interface. We fill the corresponding pore throat and body, keeping trapped wetting fluid regions unchanged to model an incompressible fluid and incorporating solid erosion and deposition following the rules described above. We then iterate through time steps until the nonwetting fluid reaches the periphery of the network or is completely surrounded by clogged pores.

IV. SOLID EROSION AND DEPOSITION ENGENDER FUNDAMENTALLY DIFFERENT DRAINAGE BEHAVIORS

As a baseline, we first establish the classic case of invasion percolation without any erosion ($\tilde{t}_d = 0$, $\tilde{\Sigma} = 0$). As expected, drainage occurs through a series of successive bursts along a ramified disordered pathway characteristic of typical CF (see movie S1 in [69]). The resulting nonwetting fluid pathway fills a fraction $\phi = \phi_{\mathrm{CF}} = 0.10 \pm 0.04$ of the total pore space volume and has a fractal dimension [70] $d_f = 1.86 \pm 0.04$ (Appendix D), in good agreement with previous studies of CF [18,19,23]. Furthermore, slightly increasing the amount of erodible material, but without any erosion ($0 < \tilde{t}_d < 0.9$, $\tilde{\Sigma} = 0$), still results in CF [see Figs. 1(e) and 1(f) and movie S2 in [69]], as expected, since in this case all pores are simply constricted uniformly. However, increasing further above a threshold value $\tilde{t}_d = \tilde{t}_d^* \approx 0.9$ causes a precipitous drop in ϕ [Figs. 1(e) and 1(f)] as pores near the inlet start off clogged, preventing fluid drainage from occurring (movie S3 in [69]). We therefore call this behavior rapid clogging.

Next we explore the case of high erodibility ($\tilde{\Sigma} = 0.8$). When the amount of material that can be eroded is small ($\tilde{t}_d \leqslant 0.1$), the influence of erosion and deposition is minimal and drainage again proceeds through typical CF [Fig. 1(g), circles]. We observe dramatically different behavior with increasing $\tilde{t}_d$. Above a threshold value $\tilde{t}_d = \tilde{t}_d^{**} \approx 0.15$, the nonwetting fluid volume fraction is larger than in CF [$\phi/\phi_{\mathrm{CF}} > 1$, Fig. 1(g), stars], that is, as more erodible material is added to the pore space, the nonwetting fluid is somehow able to form new, ramified fingers and thereby drain more of the pore space [see Figs. 1(e) and 1(g) and movie in S4 [69]]. We therefore call this behavior erosion-enhanced fingering. This surprising behavior persists with increasing $\tilde{t}_d$ until it

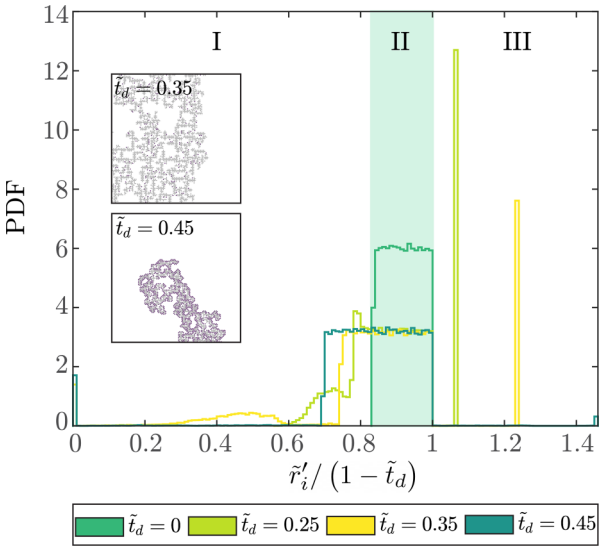

FIG. 2. Examining the probability density function (PDF) of $\tilde{r}_i'/(1-\tilde{t}_d)$, the pore sizes after drainage relative to the largest starting pore size, elucidates the origins of different drainage behaviors. We consider the representative case of strong erosion ($\tilde{\Sigma} = 0.8$) shown in Fig. 1(g). The initial uniform distribution is shown in region II for the pristine case without any erodible material ($\tilde{t}_d = 0$). Above the threshold to transition to EEF $\tilde{t}_d \approx 0.15$, two subfractions of smaller and larger pores (regions I and III) split off, reflecting pores that have had material eroded from and redeposited in, respectively. At larger $\tilde{t}_d$ above the threshold $\tilde{t}_d \approx 0.4$, increasing clogging (peak in region I) causes a transition to RC. Insets show magnified views of the resulting patterns of nonwetting fluid displacement (gray) and pore clogging (purple) for $\tilde{t}_d = 0.35$ and 0.45.

eventually becomes suppressed by pore clogging; in this case, we again observe a transition to RC, characterized by a precipitous drop in ϕ/ϕ_{CF}, above a threshold value $\tilde{t}_d = \tilde{t}_d^* \approx 0.4$ [Fig. 1(g), squares].

V. ORIGINS OF THESE DRAINAGE BEHAVIORS

Why do these fascinating drainage behaviors arise in erodible porous media? Inspecting changes in the distribution of pore sizes after drainage, which quantifies how the nonwetting fluid displacement has reshaped the pore space structure, provides a clue. In particular, we examine the distributions of $\tilde{r}_i'/(1-\tilde{t}_d) = \tilde{r}_i'/\tilde{r}_{i,\max}$, which describe the pore sizes after drainage relative to the largest starting pore size $\tilde{r}_{i,\max} \equiv \max\{\tilde{r}_i\}$. We focus on the highly erodible case of $\tilde{\Sigma} = 0.8$ described in Fig. 1(g) as a representative example. When the medium only has a little erodible material ($\tilde{t}_d < 0.15$), the initial uniform distribution of pore sizes remains unaltered (region II in Fig. 2). However, as exemplified by $\tilde{t}_d = 0.25$ in Fig. 2, just above the threshold $\tilde{t}_d^{**} \approx 0.15$, two subfractions of smaller and larger pores (regions I and III, respectively) split off from this distribution. These reflect the increasing fraction of pore throats that have had solid material eroded from and redeposited in, respectively; indeed, the eroded pores reach a uniform size set by the balance of capillarity and erosion, with $\tilde{r}_i'/\tilde{r}_{i,\max} \approx 1.1 = \tilde{\Sigma}/(1-\tilde{t}_d)$, as expected. Notably, the smaller pores still have sizes $\tilde{r}_i > 0$, indicating that they have not yet reached the threshold for clogging. We observe similar behavior in Fig. 2 for the cases of $\tilde{t}_d = 0.35$ and 0.45, for which the eroded pores now reach the expected sizes $\tilde{r}_i'/\tilde{r}_{i,\max} = \tilde{\Sigma}/(1-\tilde{t}_d) \approx 1.2$ and 1.5, respectively.

Thus, we expect that EEF begins when capillary forces become just large enough to begin eroding the solid matrix, and the redeposition of this material constricts downstream pores slightly, just enough to force the nonwetting fluid to explore new pathways through the pore space that it otherwise would not have. We quantify this expectation for the onset of EEF by balancing the smallest capillary pressure that can possibly be encountered during drainage, $\Delta p_c(r_{p,\max} - t_d^{**})$, with the threshold erosion stress σ_y. In nondimensional form, our prediction is

$$\tilde{t}_d^{**} = 1 - \tilde{\Sigma}. \tag{1}$$

This prediction yields $\tilde{t}_d^{**} = 0.2$, in good agreement with the value of $\tilde{t}_d^{**} \approx 0.15$ found from the simulations for the case of $\tilde{\Sigma} = 0.8$.

As $\tilde{t}_d$ increases above $\tilde{t}_d^{**}$, we expect that the increasing amount of erodible material increases the propensity of pores to become clogged, giving rise to the nonmonotonic variation of ϕ shown in Fig. 1(g). Consistent with this expectation, a larger fraction of pores in region I becomes clogged (shown by the growing peak at $\tilde{r}_i' = 0$, also indicated by the purple points in the insets in Fig. 2 and movies S5 and S6 in [69]). The height of the peak in region III concomitantly decreases, indicating that fewer pores are ultimately eroded.

Thus, we expect that EEF transitions to RC when pore clogging is so prevalent that it chokes off fluid drainage. We quantify this expectation for the onset of RC by balancing the volume of solid material that can be eroded from a pore i, proportional to $(2\gamma/\sigma_y)^2 - (r_{i,p} - t_d^*)^2$, with the characteristic available volume in the adjacent connected pores j, proportional to $\alpha(r_{j,p} - t_d^*)^2$, where the constant $\alpha \approx \frac{4}{3}$ accounts for the network connectivity (Appendix F). While both $r_{i,p}$ and $r_{j,p}$ are broadly distributed, we make the assumption that both are approximately $r_{p,\max}$. With this simplification, in nondimensional form, our prediction is

$$\tilde{t}_d^* = 1 - \frac{\tilde{\Sigma}}{\sqrt{1+\alpha}}. \tag{2}$$

This prediction yields $\tilde{t}_d^* = 0.4$, in excellent agreement with the value of $\tilde{t}_d^* \approx 0.4$ found from the simulations, for the case of $\tilde{\Sigma} = 0.8$.

VI. UNIFIED STATE DIAGRAM FOR DRAINAGE IN AN ERODIBLE POROUS MEDIUM

As a final test of the predictions given by Eqs. (1) and (2), we perform a total of 44 100 numerical simulations over a broad range of $(\tilde{t}_d, \tilde{\Sigma})$. We characterize the drainage pattern that emerges for each condition tested using the volume fraction and fractal dimension [70] of the nonwetting fluid pathway ϕ and d_f, respectively. Our results are summarized in Fig. 3 and Appendix D. Consistent with the observations shown in Figs. 1 and 2, CF emerges for small $(\tilde{t}_d, \tilde{\Sigma})$ (circles), transitioning to EEF for $\tilde{t}_d \geqslant \tilde{t}_d^{**}$ (stars), and then transitioning to RC for $\tilde{t}_d \geqslant \tilde{t}_d^*$ (stars). The boundaries between these distinct drainage behaviors agree well with the predictions given

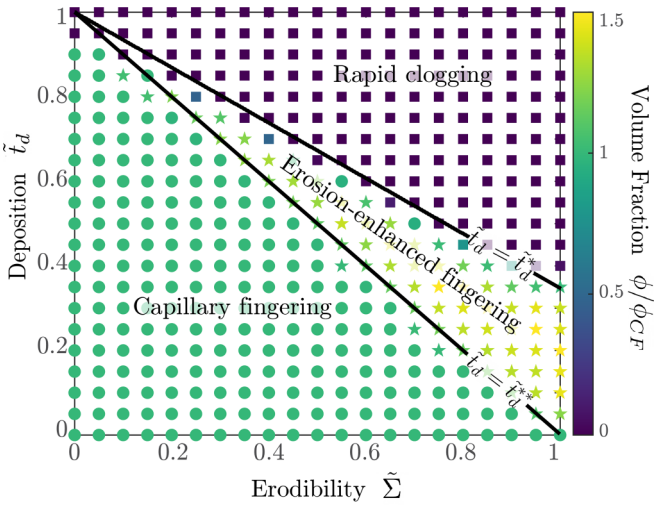

FIG. 3. State diagram of different drainage behaviors in an erodible porous medium. Colors show the normalized nonwetting fluid volume fraction ϕ/ϕ_{CF}; each symbol shows the average of 100 different simulations testing different, but statistically identical, networks. We observe the emergence of three distinct drainage behaviors: capillary fingering (circles, $0.9 < \phi/\phi_{CF} < 1$), rapid clogging (squares, $\phi/\phi_{CF} < 0.9$), and erosion-enhanced fingering (stars, $\phi/\phi_{CF} > 1$). The boundaries between these regimes, shown by the lower and upper black solid lines, are given by Eqs. (1) and (2), respectively. As shown in Appendix D, these distinct drainage behaviors can also be characterized by the distinct fractal dimensions of the resulting drainage patterns. In particular, all simulations in the CF regime are characterized by a constant fractal dimension $d_f = 1.86 \pm 0.04$. By contrast, in the EEF regime, the measured fractal dimensions are more varied, indicating that different $(\tilde{\Sigma}, \tilde{t}_d)$ combinations yield nonwetting fluid patterns with more varied ramification: We find a maximum measured fractal dimension of $d_f = 1.93 \pm 0.01$ for $(\tilde{\Sigma}, \tilde{t}_d) = (0.9, 0.4)$, indicating a slightly more compact pathway, and a minimum measured fractal dimension of $d_f = 1.71 \pm 0.05$ for $(\tilde{\Sigma}, \tilde{t}_d) = (0.15, 0.85)$, indicating a slightly more ramified pathway than capillary fingering.

by Eqs. (1) and (2), shown by the lower and upper solid lines in Fig. 3, respectively, despite the simplifying assumptions made therein. Thus, not only has our extended model of invasion percolation shown that the coupling between nonwetting fluid displacement and solid erosion and deposition engender fascinating drainage behaviors, but our analysis provides quantitative principles to help predict when they arise.

VII. CONCLUSION

To our knowledge, these different drainage behaviors have never been observed in experiments. Our predictions provide guidelines for future studies to search for them. For example, 2D microfluidic channels could be designed to mimic the pore networks studied here [71], with a fixed thickness t_d of colloidal particles or polymeric material coating the inner walls prior to drainage; the threshold stress for erosion σ_y could then be tuned by changing the physicochemical interactions between the particles or polymers and the walls. With increasing amounts of this erodible material, we predict a transition from CF to EEF and ultimately to RC, during drainage.

Inherent in our model are simplifications and approximations, as with all theoretical models. Future work could build on the framework developed here by exploring a broader range of fluid viscosity ratios [29] and flow rates (extending Lenormand's classic phase diagram [72]), as well as different forms of pore space structure and dimensionality [33,73–80], and different rules for erosion, clogging, and potential clog erosion as described further in Appendixes A–C. Ultimately, such extensions of our work could lead to improved prediction and control of coupled fluid and solid transport in diverse environmental and industrial media.

ACKNOWLEDGMENTS

It is a pleasure to acknowledge I. C. Bourg, H. A. Stone, and S. Torquato for stimulating discussions, as well as N. Bizmark, E. Y. Chen, A. Hancock, and N. Subraveti for helpful feedback on the manuscript. This work was supported by funding from the New Jersey Water Resources Research Institute, the ReMatch+ program (to C.A.Q.), a Mary and Randall Hack Graduate Award of the High Meadows Environmental Institute (to J.S.), a Maeder Graduate Fellowship from the Andlinger Center for Energy and the Environment (to J.S.), a Camille Dreyfus Teacher-Scholar Award from the Camille and Henry Dreyfus Foundation (to S.S.D.), and the Princeton Center for Complex Materials, a National Science Foundation (NSF) Materials Research Science and Engineering Center funded through NSF Grant No. DMR-2011750. This material is also based upon work by S.S.D. supported by the U.S. Department of Energy's Office of Energy Efficiency and Renewable Energy under the Geothermal Technologies Office Innovative Methods to Control Hydraulic Properties of Enhanced Geothermal Systems Award No. DE-EE0009790.

APPENDIX A: INFLUENCE OF THE NATURE OF THE DRIVING FORCE FOR DRAINAGE

In practice, the driving force for drainage can be either an imposed flow rate starting at the central injection point or a pressure drop between the injection point and periphery of the medium. However, our work explores the limit in which capillary forces dominate over other forces, including the driving force, characteristic of many real-world settings. In particular, our work examines the commonly investigated limit in which two criteria hold.

First, the threshold capillary pressure difference across the immiscible fluid interface $\Delta p_c \sim \gamma/r$ is much larger than the viscous pressure drop across a pore $\Delta p_{v,\mathrm{nw}} \sim \mu_{\mathrm{nw}} q/r$; here γ is the interfacial tension, r is the characteristic pore size, μ_{nw} is the dynamic shear viscosity of the invading nonwetting fluid, and q is the characteristic flow speed given by the Darcy velocity $q = Q/A$, where Q is the volumetric flow rate and A is the cross-sectional area of a three-dimensional medium. The ratio of these defines what is commonly referred to as the capillary number $\mathrm{Ca} \equiv \mu_{\mathrm{nw}} q/\gamma$, which is typically much less than 1 in all the applications that motivate our work.

Second, the dynamic shear viscosity of the invading nonwetting fluid μ_{nw} is much larger than that of the displaced wetting fluid μ_w. The ratio of these defines the parameter $M \equiv \mu_{\mathrm{nw}}/\mu_w$, which is often much greater than 1 in the

applications that motivate our work. Therefore, any viscous pressure gradient that may arise during flow will be primarily in the nonwetting fluid, not the displaced wetting fluid.

In this limit, regardless of the driving force for invasion (imposed pressure drop or flow rate), the fluid displacement proceeds sequentially, one pore at a time, and is solely determined by the geometry of the pore space; specifically, at each step of the drainage process, the nonwetting fluid invades the largest pore accessible to it, characterized by the lowest capillary pressure threshold, bursting through until it reaches the next pore. That this sequential invasion process is dictated by pore geometry, and not the driving force, has been verified in numerous previous studies (e.g., Refs. [18,21–34]) and thus has been the convention in the field since the seminal model of invasion percolation was developed by Wilkinson and Willemsen four decades ago [20]. Consequently, the exact nature of the driving force does not play a role in the simulations and therefore is not explicitly specified in such studies. We also note that while wetting film effects may also play a role during drainage, they are neglected from our model for simplicity and would be interesting to explore in future work.

With the addition into the model of (i) erosion of material by the invading fluid interface and (ii) deposition of eroded material downstream of the fluid interface, the nature of the driving force may play a role in the drainage process. However, given the limit of capillary-dominated displacement of a low-viscosity wetting fluid considered in our present work, possible coupling between erosion/deposition and viscous forcing likely does not play an important role in determining the key physics. Specifically, as noted above, given that $M \gg 1$, any viscous pressure gradient that may arise during flow will be primarily in the nonwetting fluid, not the displaced wetting fluid. Thus, erosion and/or deposition of material downstream of the invading fluid interface in the wetting fluid (where it could influence subsequent fluid displacement) will likely not be affected by coupling with viscous forcing. Put another way, our work focuses on the limit in which the pore-scale viscous pressure drops in the displaced wetting fluid $\Delta p_{v,w} \sim \mu_w q/r = \Delta p_{v,\mathrm{nw}}/\mathrm{M} \ll 1$, since $\mathrm{M} \gg 1$, and therefore is much smaller than the threshold yield stress σ_y required to erode material from the pore walls. The ratio between σ_y and $\Delta p_{v,w}$ defines another dimensionless parameter often known as the Bingham number, Bm, which in our work is much greater than 1. Nevertheless, the added complexity of possible coupling between fluid forcing and erosion/deposition (and clogging) may play a role in many real-life scenarios, and incorporating it into our model will be an important extension of our theoretical framework.

APPENDIX B: PHYSICAL MECHANISMS UNDERLYING SOLID EROSION AND DEPOSITION

As noted in the main text, the influence of solid erosion and deposition on fluid drainage in porous media comprised of interconnected networks of many different pores (and vice versa) has, to our knowledge, never been studied before. However, the interplay between solid erosion and deposition and fluid stresses has been examined in studies of individual pores and on flat surfaces, and the assumptions of our model are based on the findings of these studies. In particular, our model builds on these established results and extends them to larger-scale porous media, in which the coupling between solid erosion and deposition and fluid flow/capillary stresses at the pore scale, and transport across multiply connected pores, leads to the fascinating drainage behaviors revealed by our study. Below we elaborate on the physical assumptions inherent in the model and the support from prior studies for them.

First, we describe the mechanisms of erosion due to capillary stress. As noted in Appendix A, our model considers the capillary-dominated limit encountered in many real-world settings, in which capillary stresses that arise at the immiscible interface between the invading nonwetting and displaced wetting fluids dominate over viscous stresses arising from fluid flow. In this limit, prior studies in have shown that these capillary stresses can erode solid material from a surface in two ways.

(1) As the three-phase (solid surface/wetting fluid/nonwetting fluid) contact line moves, solid material protruding from the surface, e.g., predeposited colloidal particles, inorganic precipitates, and organic matter, blocks the contact line, causing thinning and rupture of the wetting liquid film formed between the immiscible fluid interface and the protrusion and eventually forming a three-phase contact line on the protrusion at which the capillary force $F_\gamma \sim \gamma d$ acts; here γ is the interfacial tension between the fluids and d is the characteristic size of the solid protrusion. This capillary-induced lift force (as it is often called) is often many orders of magnitude larger than the force F_a keeping the protrusion adhered to the solid, driving erosion. This mechanism of erosion driven by a moving immiscible fluid interface has been mathematically analyzed in [59], corroborated by simulations [60], and validated in numerous experimental studies in simplified geometries of erosion of predeposited colloidal particles [60–63] and even bacteria [66] from a solid surface.

(2) The balance of interfacial energies at the three-phase contact line has a horizontal component, which yields the classic Young-Dupré equation for the contact angle, but also has a vertical component γ_{ow}, which pulls up on the underlying substrate by a spatial extent $z \sim \gamma_{ow}/\sigma_y$ [38], where σ_y is the yield stress of the material composing the substrate. While extensive experimental tests of this mechanism are still required, the model of [38] suggests that capillary forces can yield and erode material from a solid substrate if σ_y if sufficiently small.

Taken together, these prior calculations, simulations, and experiments indicate that purely capillary stresses, such as those considered in our model, can erode material from a solid surface when the capillary pressure exceeds a threshold yield stress characterizing the material, as formulated in our model. It is important to note that the complex physics involved at the instant of erosion of solid material does not play a role in our model; it simply assumes that erosion will happen, driven by capillary stresses during drainage as detailed above. The model then explores what the consequences of this process are on subsequent drainage after the eroded material has been redeposited, using the established formalism of pore-network modeling of drainage. Thus, while unraveling the complex physics associated with the process of detaching material will certainly be a useful direction for future

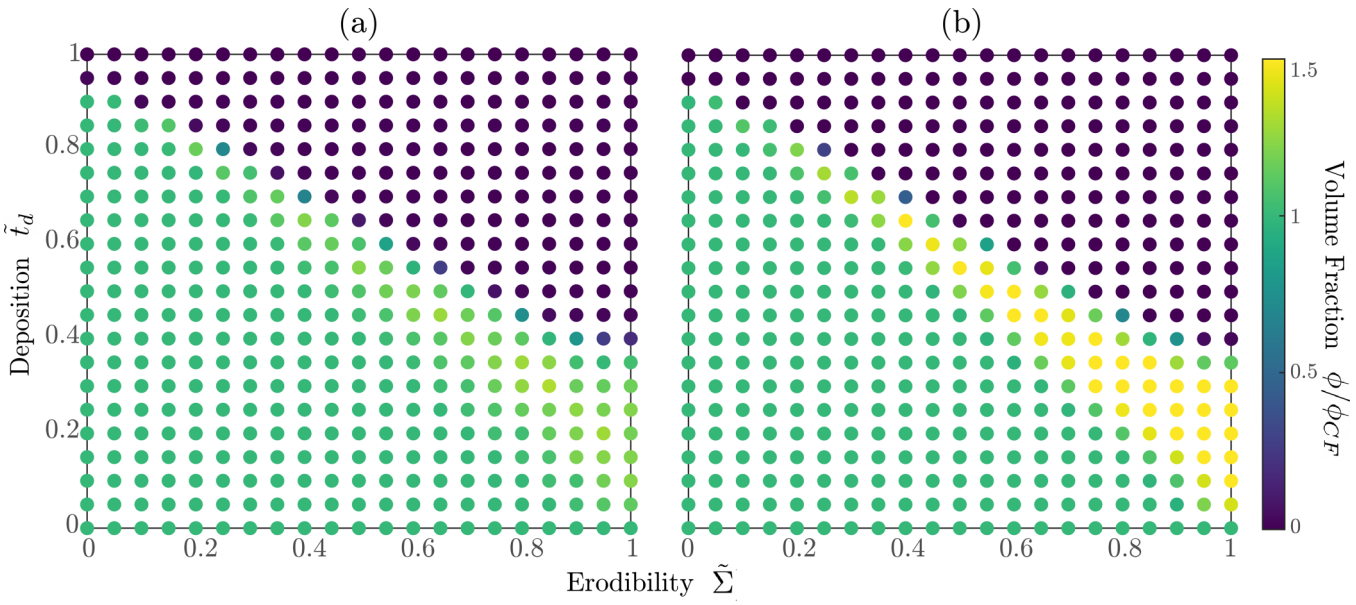

FIG. 4. Additional state diagrams of nonwetting fluid filled volume fraction ϕ/ϕ_{CF} for networks with (a) $N = 100$ and (b) $N = 300$, across the full range of deposition $\tilde{t}_d$ and erodibility $\tilde{\Sigma}$ values. For both system sizes, we again observe the emergence of capillary fingering, rapid clogging, and erosion-enhanced fingering, with the boundaries between these different drainage behaviors remaining unchanging and in good agreement with the results shown in the main text. The magnitude of ϕ/ϕ_{CF} increases slightly and then converges to $\phi/\phi_{\mathrm{CF}} \approx 1.7$ with increasing N.

work, our model does not explicitly address or rely on those details.

Next we describe the physical origin of the deposition process. There are two distinct forms of deposition considered in our model: (i) the initial coating of the inner walls of each pore throat of the medium by a layer of erodible material of initially fixed thickness and (ii) the subsequent deposition of the eroded material downstream of the moving immiscible fluid interface at which erosion occurs.

Form (i) describes the initial condition of our model, taken to be a pore network that is saturated with the wetting fluid, prior to any possible erosion by capillary stresses arising from drainage by a nonwetting fluid. In practice, the material that is initially deposited on the walls of the medium could

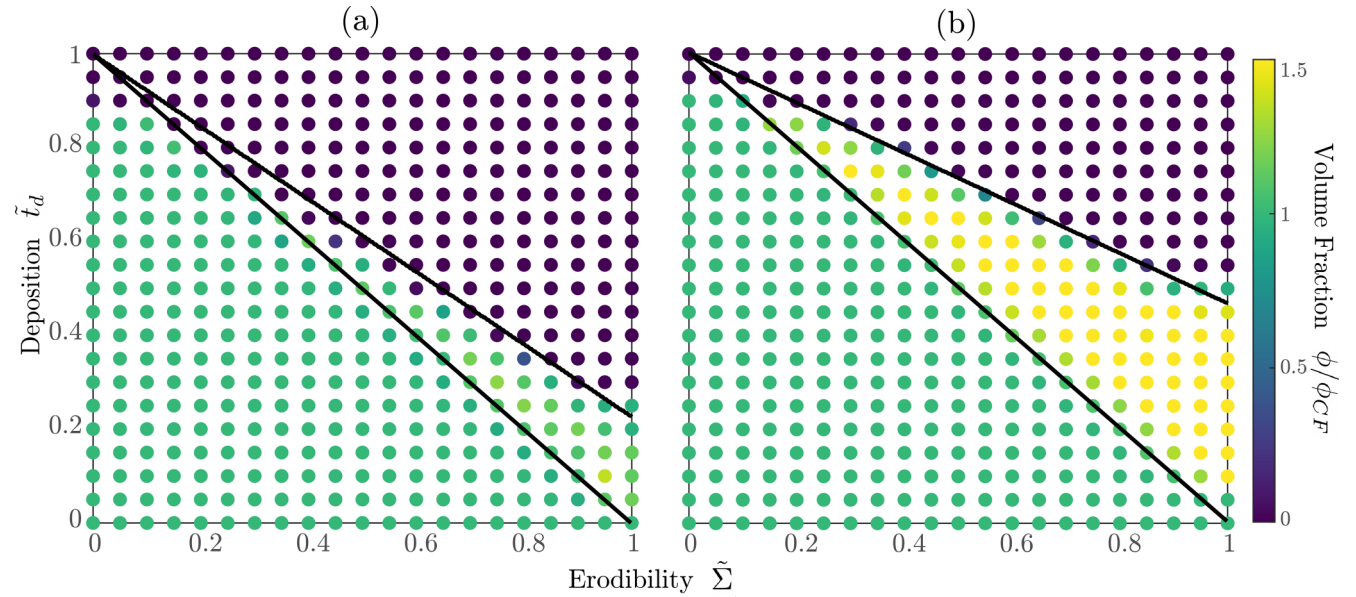

FIG. 5. Additional state diagrams of nonwetting fluid filled volume fraction ϕ/ϕ_{CF} for networks with connectivity (a) $c = 3$ and (b) $c = 6$, across the full range of deposition $\tilde{t}_d$ and erodibility $\tilde{\Sigma}$ values. In both cases, we again observe the emergence of capillary fingering, rapid clogging, and erosion-enhanced fingering, as in the main text. The erosion-enhanced fingering regime spans a smaller (larger) range of $(\tilde{t}_d, \tilde{\Sigma})$ and the corresponding ϕ/ϕ_{CF} is smaller (larger) for the case of $c = 3$ ($c = 6$). These changes are captured by our theory when we account for network connectivities. When $c = 3$, $\alpha = \frac{2}{3}$, and when $c = 6$, $\alpha = \frac{5}{2}$.

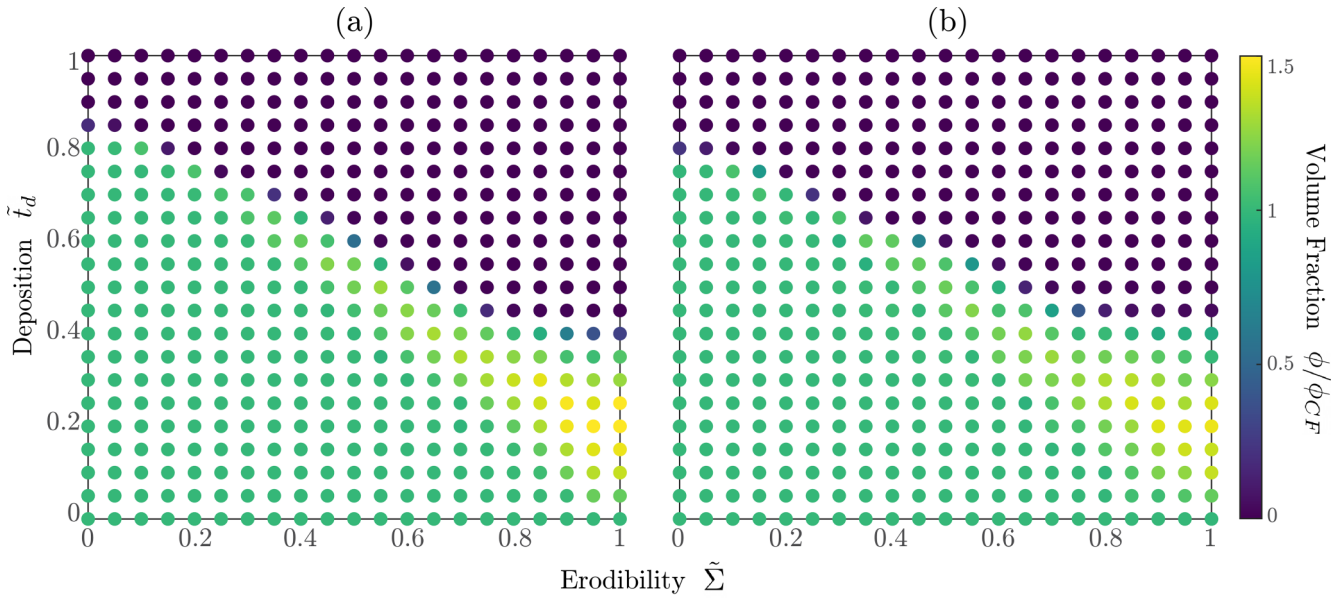

FIG. 6. Additional state diagrams of nonwetting fluid filled volume fraction ϕ/ϕ_{CF} for wider uniform distributions, (a) $\tilde{r}_{i,p} \in [0.68, 1]$ and (b) $\tilde{r}_{i,p} \in [0.58, 1]$, across the full range of deposition $\tilde{t}_d$ and erodibility $\tilde{\Sigma}$ values. In both cases, we again observe the emergence of capillary fingering, rapid clogging, and erosion-enhanced fingering, as in the main text. The erosion-enhanced fingering regime spans a smaller range of $(\tilde{t}_d, \tilde{\Sigma})$ as the distributions become wider.

be, e.g., colloidal clay or silica particles, inorganic precipitates, and organic matter, which are typically transported from the wetting fluid via passive diffusion or fluid advection and attach to the pore walls due to adhesive forces such as van der Waals attraction or entropic depletion attraction (see, e.g., [58] for more details). In this case, as noted earlier, given that our model considers the capillary-dominated limit in which erosion is solely determined by capillary stresses, there is no erosion.

Form (ii) describes the process by which eroded material, due to capillary stresses, as described above, is redeposited downstream of the fluid interface. In practice, this redeposition process again arises due to transport of eroded material in the wetting fluid downstream of the invading immiscible fluid interface via passive diffusion or fluid advection, followed by subsequent reattachment to the downstream pore walls due to adhesive forces such as van der Waals attraction or entropic depletion attraction. Therefore, our model simply distributes the volume eroded from a given pore to the downstream pores following mass conservation.

Much work remains to be done to completely unravel the complexities associated with solid erosion and deposition in porous media. Nevertheless, the assumptions inherent in our model provide a simple way of capturing the essential physics of erosion of deposited material by capillary forces, and redeposition of that eroded material, in a manner that is motivated by the physical arguments presented above, as well as the results of the prior theoretical, computational, and experimental studies noted above.

APPENDIX C: DISTRIBUTION OF ERODED MATERIAL ACROSS ADJACENT CONNECTED PORES

To estimate how much material eroded from drained throat i is redeposited into the nondrained throats j that are directly connected to it, we consider the pressure drop δp_j across each of j. Because the length of an individual pore throat, assumed to be uniform throughout the network, is much smaller than the overall length of the pore network (i.e., $N \gg 1$), we assume that δp_j is approximately constant across each downstream pore j, as given by the Hagen-Poiseuille equation. Thus, the flux of material into each throat j is proportionate to r_j^4; we therefore assume that the new volume added to each of the n connected throats j, δV_j, after a volume V_{erode} is eroded by drainage in throat i is given by $\delta V_j = \frac{r_j^4}{\sum_{k=1}^{n} r_k^4} V_{\mathrm{erode}}$. However, if δV_j causes $\tilde{r}_j < 0$, the excess volume is returned to the drained throat i to conserve mass. This implementation represents a simple possible choice that explicitly incorporates differences in the flux of redeposited material due to differences in pore geometry; exploring the influence of other choices, such as by making redeposition proportional instead to the throat areas, could be interesting to explore in future work.

APPENDIX D: SIMILARITY OF RESULTS WITH VARYING PARAMETERS

Figures 4–7 show results similar to those described in Fig. 3 of the main text but for other values of N, c, and forms of $\rho(\tilde{r}_{i,p})$, including those obtained from real-world media. Furthermore, Fig. 8 shows data obtained from the same simulations as in Fig. 3 but instead showing the fractal dimension d_f of the nonwetting fluid displacement pathway after drainage through the medium has concluded.

APPENDIX E: INSENSITIVITY OF OUR RESULTS TO THE CHOICE OF INJECTION CONDITIONS

In many of the applications that motivate our work, fluid invasion starts from a surface on one edge, including in

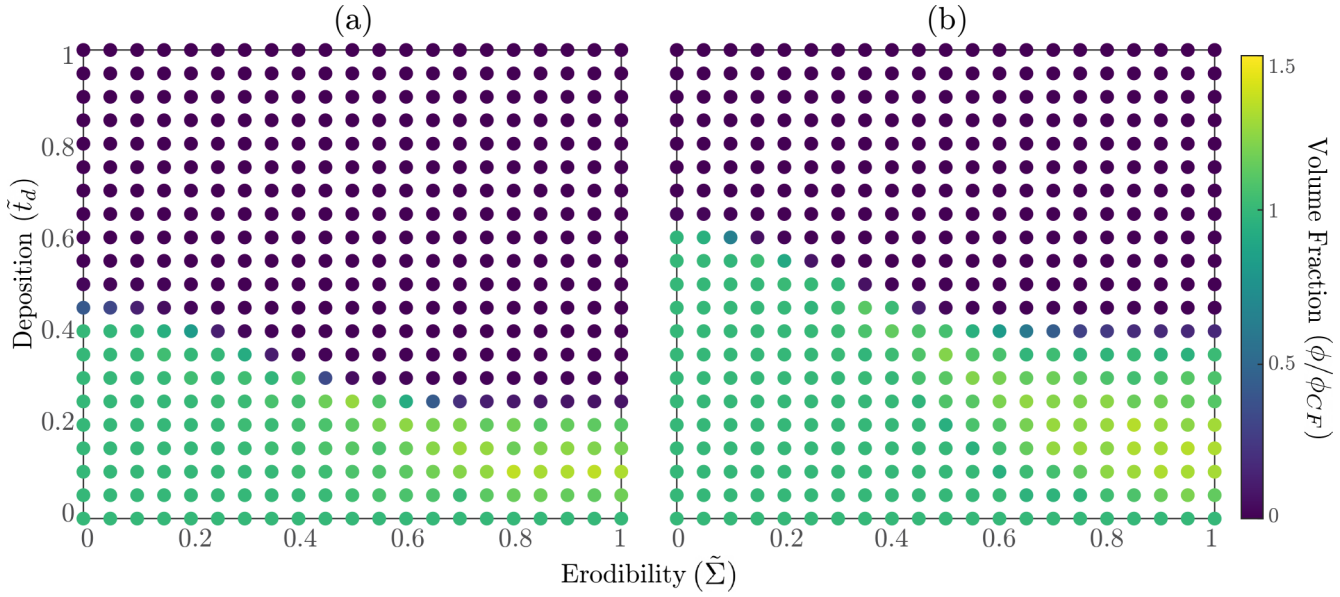

FIG. 7. Additional state diagrams of nonwetting fluid filled volume fraction ϕ/ϕ_{CF} for nonuniform $\rho(r_{i,p})$ that are representative of two real-world examples as obtained from [81]: (a) Berea sandstone and (b) a monodisperse bead packing. The Berea sandstone has $\rho(r_{i,p}) = \frac{15}{4(r_{\max}-r_{\min})}(1-\frac{r_{i,p}-r_{\min}}{r_{\max}-r_{\min}})\sqrt{\frac{r_{i,p}-r_{\min}}{r_{\max}-r_{\min}}}$, with $r_{\min} = 1\,\mu\mathrm{m}$ and $r_{\max} = 25\,\mu\mathrm{m}$. The bead packing has $\rho(r_{i,p}) = \frac{6}{(r_{\max}-r_{\min})}\sqrt{\frac{r_{i,p}-r_{\min}}{r_{\max}-r_{\min}}}\sqrt{1-\frac{r_{i,p}-r_{\min}}{r_{\max}-r_{\min}}}$, with $r_{\min} = 15\,\mu\mathrm{m}$ and $r_{\max} = 40\,\mu\mathrm{m}$. In both cases, we again observe the emergence of capillary fingering, rapid clogging, and erosion-enhanced fingering, as in the main text.

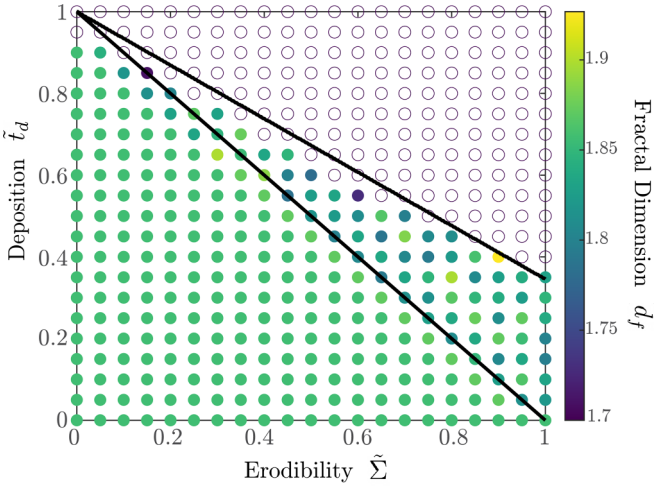

FIG. 8. State diagram for the same simulations as in Fig. 3 but instead showing the fractal dimension d_f of the nonwetting fluid displacement pathway after drainage through the medium has concluded. As in Fig. 3, each symbol shows the average of 100 different simulations testing different, but statistically identical, networks. The capillary fingering regime is characterized by a constant fractal dimension $d_f = 1.86 \pm 0.04$. However, in the erosion-enhanced fingering regime, the measured fractal dimensions are more varied, indicating that different $(\tilde{\Sigma}, \tilde{t}_d)$ combinations yield nonwetting fluid patterns with more varied ramification: We find a maximum measured fractal dimension of $d_f = 1.93 \pm 0.01$ for $(\tilde{\Sigma}, \tilde{t}_d) = (0.9, 0.4)$, indicating a slightly more compact pathway, and a minimum measured fractal dimension of $d_f = 1.71 \pm 0.05$ for $(\tilde{\Sigma}, \tilde{t}_d) = (0.15, 0.85)$, indicating a slightly more ramified pathway than capillary fingering. The open circles indicate the rapid clogging regime, in which the filled volume fraction of the pore network is too low to accurately obtain d_f.

soil drying and in gas venting from sediments. In other applications, such as groundwater remediation, enhanced oil recovery, and CO_2 sequestration, fluid injection from a well bore into a porous subsurface rock is instead better represented using a central starting invasion point in which the immiscible fluid spreads out radially. Thus, both invasion conditions arise in real-world settings.

As a result, fluid invasion starting from a central position (as we use in our work) is a convention in this field, although invasion from an edge is also commonly studied. References [35,68] provide two representative examples of invasion percolation studied using the former approach (invasion from a central position), whereas seminal studies of invasion percolation in the 1980s, e.g., Refs. [20,23], used the latter approach (invasion from one edge). Notably, the fractal dimension of capillary fingering that results from traditional invasion percolation is consistent across both sets of references (and with our findings), suggesting that the results of simulations performed using either invasion condition are equivalent.

Nevertheless, to confirm this equivalence more directly, we also performed simulations representative of the three drainage behaviors characterized by our work, i.e., capillary fingering, rapid clogging, and erosion-enhanced fingering, but with fluid invasion from one edge. The results of these simulations, shown in movies S7–S9 in [69], show that the features of these drainage behaviors are consistent across both invasion conditions.

APPENDIX F: ONSET OF RAPID CLOGGING

To estimate when pore clogging is so prevalent that it chokes off fluid drainage, causing irreversible clogging, we

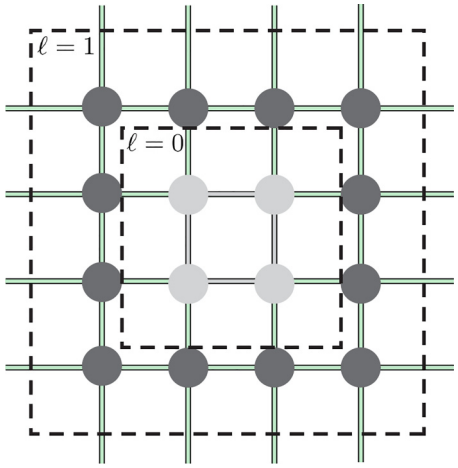

FIG. 9. Schematic of fluid drainage proceeding from the initialization of a simulation. The light gray pore bodies connected by light gray pore throats represent the injection source used in all simulations. The pore throats in layer 0, labeled $\ell = 0$, are invaded to fill the first layer of pore bodies, shown in darker gray ($\ell = 1$). The volume eroded from the pore bodies in the first layer is then eroded into its connected pore throats, which are shown in mint green. We expect clogging to occur at $\ell = 1$, when the ratio of available pore throats to previously invaded pore bodies provides a value of $\alpha = \frac{4}{3}$.

balance the volume of solid material that can be eroded from a pore i, $V_{\text{erode}} \propto (2\gamma/\sigma_y)^2 - (r_{i,p} - t_d^*)^2$, with the cumulative total available volume in the adjacent connected nondrained pore throats j, $V_{\text{available}} \propto (r_{j,p} - t_d^*)^2$. For tractability of computation, we make the assumption that both $r_{i,p}$ and $r_{j,p} \sim r_{p,\max}$. Thus $V_{\text{erode}} \propto \tilde{\Sigma}^2 - (1 - \tilde{t}_d^*)^2$ and $V_{\text{available}} \propto (1 - \tilde{t}_d^*)^2$. This assumption that $r_{i,p}, r_{j,p} \sim r_{p,\max}$ allows us to make the approximation that fluid drainage will expand radially in sequential annular layers from the central injection point (Fig. 9), as opposed to the ramified invasion patterns typical of invasion percolation. On a square lattice of connectivity $c = 4$, layer ℓ experiences $8\ell + 4$ invasions, yielding a total eroded volume $(8\ell + 4)V_{\text{erode}}$, which gets redeposited onto $8(\ell + 1)$ available pore throats with a total available volume of $8(\ell + 1)V_{\text{available}}$. Thus, taking a mean-field approximation layer by layer, we expect clogging to occur at $\ell = 1$ when $(8\ell + 4)V_{\text{erode}} \sim 8(\ell + 1)V_{\text{available}}$, or $V_{\text{erode}} \sim \frac{4}{3}V_{\text{available}}$.

The same result can similarly be obtained for lattices with $c = 3$ and 6. For a lattice with connectivity $c = 3$, layer ℓ experiences $6(2\ell + 1)$ invasions, yielding a total eroded volume $6(2\ell + 1)V_{\text{erode}}$, which gets redeposited onto $6(\ell + 1)$ available pore throats with a total available volume of $6(\ell + 1)V_{\text{available}}$. If we similarly expect clogging to occur at $\ell = 1$, $V_{\text{erode}} \sim \frac{2}{3}V_{\text{available}}$ [Fig. 5(a)]. For a lattice with connectivity $c = 6$, layer ℓ experiences $6\ell + 6$ invasions, yielding a total eroded volume $(6\ell + 6)V_{\text{erode}}$, which gets redeposited onto $12(\ell + 1) + 6$ available pore throats with a total available volume of $[12(\ell + 1) + 6]V_{\text{available}}$. If we similarly expect clogging to occur at $\ell = 1$, $V_{\text{erode}} \sim \frac{5}{2}V_{\text{available}}$ [Fig. 5(b)].

[1] C. M. Bethke, J. D. Reed, and D. F. Oltz, Long-range petroleum migration in the Illinois basin, AAPG Bull. **75**, 925 (1991).

[2] B. H. Kueper and E. O. Frind, Two-phase flow in heterogeneous porous media: 1. Model development, Water Resour. Res. **27**, 1049 (1991).

[3] H. E. Dawson and P. V. Roberts, Influence of viscous, gravitational, and capillary forces on DNAPL saturation, Groundwater **35**, 261 (1997).

[4] L. C. Levy, P. J. Culligan, and J. T. Germaine, Modelling of DNAPL behavior in vertical fractures, Int. J. Phys. Model. Geo. **3**, 01 (2003).

[5] A. Y. Dandekar, *Petroleum Reservoir Rock and Fluid Properties* (CRC, Boca Raton, 2006).

[6] S. M. Benson and F. M. Orr, Carbon dioxide capture and storage, MRS Bull. **33**, 303 (2008).

[7] L. Cueto-Felgueroso and R. Juanes, Nonlocal interface dynamics and pattern formation in gravity-driven unsaturated flow through porous media, Phys. Rev. Lett. **101**, 244504 (2008).

[8] J. A. Neufeld and H. E. Huppert, Modelling carbon dioxide sequestration in layered strata, J. Fluid Mech. **625**, 353 (2009).

[9] J. Bear and A. H.-D. Cheng, *Modeling Groundwater Flow and Contaminant Transport* (Springer, Berlin, 2010), Vol. 23.

[10] C. W. MacMinn, M. L. Szulczewski, and R. Juanes, CO_2 migration in saline aquifers. Part 1. Capillary trapping under slope and groundwater flow, J. Fluid Mech. **662**, 329 (2010).

[11] E. Saadatpoor, S. L. Bryant, and K. Sepehrnoori, New trapping mechanism in carbon sequestration, Transp. Porous Media **82**, 3 (2010).

[12] U. C. Bandara, A. M. Tartakovsky, and B. J. Palmer, Pore-scale study of capillary trapping mechanism during CO_2 injection in geological formations, Int. J. Greenh. Gas Con. **5**, 1566 (2011).

[13] M. Sahimi, *Flow and Transport in Porous Media and Fractured Rock: From Classical Methods to Modern Approaches* (Wiley, New York, 2011).

[14] S. Berg and H. Ott, Stability of CO_2-brine immiscible displacement, Int. J. Greenh. Gas Con. **11**, 188 (2012).

[15] M. Carmo, D. L. Fritz, J. Mergel, and D. Stolten, A comprehensive review on PEM water electrolysis, Int. J. Hydrogen Energ. **38**, 4901 (2013).

[16] C. H. Lee, R. Banerjee, F. Arbabi, J. Hinebaugh, and A. Bazylak, *International Conference on Nanochannels, Microchannels, and Minichannels* (American Society of Mechanical Engineers, New York, 2016), Vol. 50343, p. V001T07A003.

[17] H. Bazyar, P. Lv, J. A. Wood, S. Porada, D. Lohse, and R. G. Lammertink, Liquid-liquid displacement in slippery liquid-infused membranes (slims), Soft Matter **14**, 1780 (2018).

[18] M. Knackstedt and L. Paterson, Invasion percolation, in *Encyclopedia of Complexity and Systems Science*, edited by R. A. Meyers (Springer, New York, 2009), pp. 4947–4960.

[19] M. J. Blunt, *Multiphase Flow in Permeable Media: A Pore-Scale Perspective* (Cambridge University Press, Cambridge, 2017).

[20] D. Wilkinson and J. F. Willemsen, Invasion percolation: A new form of percolation theory, J. Phys. A: Math. Gen. **16**, 3365 (1983).

[21] R. P. Mayer and R. A. Stowe, Mercury porosimetry—breakthrough pressure for penetration between packed spheres, J. Colloid Sci. **20**, 893 (1965).

[22] R. Lenormand, C. Zarcone, and A. Sarr, Mechanisms of the displacement of one fluid by another in a network of capillary ducts, J. Fluid Mech. **135**, 337 (1983).

[23] R. Lenormand and C. Zarcone, Invasion percolation in an etched network: Measurement of a fractal dimension, Phys. Rev. Lett. **54**, 2226 (1985).

[24] G. Mason and N. Morrow, Meniscus displacement curvatures of a perfectly wetting liquid in capillary pore throats formed by spheres, J. Colloid Interface Sci. **109**, 46 (1986).

[25] R. Lenormand and C. Zarcone, Capillary fingering: Percolation and fractal dimension, Transp. Porous Media **4**, 599 (1989).

[26] N. Martys, M. Cieplak, and M. O. Robbins, Critical phenomena in fluid invasion of porous media, Phys. Rev. Lett. **66**, 1058 (1991).

[27] K. J. Måløy, L. Furuberg, J. Feder, and T. Jøssang, Dynamics of slow drainage in porous media, Phys. Rev. Lett. **68**, 2161 (1992).

[28] P. G. Toledo, L. Scriven, and H. T. Davis, Pore-space statistics and capillary pressure curves from volume-controlled porosimetry, SPE Formation Eval. **9**, 46 (1994).

[29] B. Xu, Y. C. Yortsos, and D. Salin, Invasion percolation with viscous forces, Phys. Rev. E **57**, 739 (1998).

[30] L. Xu, S. Davies, A. B. Schofield, and D. A. Weitz, Dynamics of drying in 3D porous media, Phys. Rev. Lett. **101**, 094502 (2008).

[31] V. Joekar-Niasar and S. Hassanizadeh, Analysis of fundamentals of two-phase flow in porous media using dynamic pore-network models: A review, Crit. Rev. Env. Sci. Tec. **42**, 1895 (2012).

[32] A. T. Krummel, S. S. Datta, S. Münster, and D. A. Weitz, Visualizing multiphase flow and trapped fluid configurations in a model three-dimensional porous medium, AIChE J. **59**, 1022 (2013).

[33] S. S. Datta and D. A. Weitz, Drainage in a model stratified porous medium, Europhys. Lett. **101**, 14002 (2013).

[34] S. S. Datta, T. Ramakrishnan, and D. A. Weitz, Mobilization of a trapped non-wetting fluid from a three-dimensional porous medium, Phys. Fluids **26**, 022002 (2014).

[35] R. Holtzman and R. Juanes, Crossover from fingering to fracturing in deformable disordered media, Phys. Rev. E **82**, 046305 (2010).

[36] R. Holtzman, M. L. Szulczewski, and R. Juanes, Capillary fracturing in granular media, Phys. Rev. Lett. **108**, 264504 (2012).

[37] N. J. Derr, D. C. Fronk, C. A. Weber, A. Mahadevan, C. H. Rycroft, and L. Mahadevan, Flow-driven branching in a frangible porous medium, Phys. Rev. Lett. **125**, 158002 (2020).

[38] R. W. Style, L. Isa, and E. R. Dufresne, Adsorption of soft particles at fluid interfaces, Soft Matter **11**, 7412 (2015).

[39] J. Means and R. Wuayaratne, Role of natural colloids in the transport of hydrophobic pollutants, Science **215**, 968 (1982).

[40] E. Tipping and D. Higgins, The effect of adsorbed humic substances on the colloid stability of haematite particles, Colloids Surf. **5**, 85 (1982).

[41] R. J. Gibbs, Effect of natural organic coatings on the coagulation of particles, Environ. Sci. Technol. **17**, 237 (1983).

[42] M. Y. Corapcioglu and S. Jiang, Colloid-facilitated groundwater contaminant transport, Water Resour. Res. **29**, 2215 (1993).

[43] Y. Ouyang, D. Shinde, R. Mansell, and W. Harris, Colloid-enhanced transport of chemicals in subsurface environments: A review, Crit. Rev. Env. Sci. Tec. **26**, 189 (1996).

[44] L. Hendraningrat, B. Engeset, S. Suwarno, S. Li, and O. Torsæter, International Symposium of the Society of Core Analysts, Napa Valley, 2013 (unpublished), paper SCA2013-062, pp. 16–19.

[45] S. Feia, J. C. Dupla, S. Ghabezloo, J. Sulem, J. Canou, A. Onaisi, H. Lescanne, and E. Aubry, Experimental investigation of particle suspension injection and permeability impairment in porous media, Geomech. Energy Env. **3**, 24 (2015).

[46] G. Gerber, M. Bensouda, D. A. Weitz, and P. Coussot, Self-limited accumulation of colloids in porous media, Phys. Rev. Lett. **123**, 158005 (2019).

[47] N. Bizmark, J. Schneider, R. D. Priestley, and S. S. Datta, Multiscale dynamics of colloidal deposition and erosion in porous media, Sci. Adv. **6**, eabc2530 (2020).

[48] G. Gerber, D. A. Weitz, and P. Coussot, Propagation and adsorption of nanoparticles in porous medium as traveling waves, Phys. Rev. Res. **2**, 033074 (2020).

[49] L. Li, Y. Su, Y. Lv, and J. Tu, Asphaltene deposition and permeability impairment in shale reservoirs during CO_2 huff-n-puff EOR process, Petrol. Sci. Technol. **38**, 384 (2020).

[50] J. McCarthy and J. Zachara, ES&T features: Subsurface transport of contaminants, Environ. Sci. Technol. **23**, 496 (1989).

[51] A. T. Kan and M. B. Tomson, Ground water transport of hydrophobic organic compounds in the presence of dissolved organic matter, Environ. Toxicol. Chem. **9**, 253 (1990).

[52] W. P. Johnson and B. E. Logan, Enhanced transport of bacteria in porous media by sediment-phase and aqueous-phase natural organic matter, Water Resour. **30**, 923 (1996).

[53] A. Franchi and C. R. O'Melia, Effects of natural organic matter and solution chemistry on the deposition and reentrainment of colloids in porous media, Environ. Sci. Technol. **37**, 1122 (2003).

[54] A. J. Pelley and N. Tufenkji, Effect of particle size and natural organic matter on the migration of nano- and microscale latex particles in saturated porous media, J. Colloid Interface Sci. **321**, 74 (2008).

[55] D. Wilkinson, Percolation effects in immiscible displacement, Phys. Rev. A **34**, 1380 (1986).

[56] A. Birovljev, L. Furuberg, J. Feder, T. Jssang, K. J. Mly, and A. Aharony, Gravity invasion percolation in two dimensions: Experiment and simulation, Phys. Rev. Lett. **67**, 584 (1991).

[57] Y. Masson, A fast two-step algorithm for invasion percolation with trapping, Comput. Geosci. **90**, 41 (2016).

[58] R. Kretzschmar and H. Sticher, Colloid transport in natural porous media: Influence of surface chemistry and flow velocity, Phys. Chem. Earth **23**, 133 (1998).

[59] S. B. G. O'Brien and B. H. A. A. Van Den Brule, A mathematical model for the cleansing of silicon substrates by fluid immersion, J. Colloid Interface Sci. **144**, 210 (1991).

[60] T. Yin, D. Shin, J. Frechette, C. E. Colosqui, and G. Drazer, Dynamic effects on the mobilization of a deposited nanoparticle by a moving liquid-liquid interface, Phys. Rev. Lett. **121**, 238002 (2018).

[61] P. Sharma, M. Flury, and J. Zhou, Detachment of colloids from a solid surface by a moving air-water interface, J. Colloid Interface Sci. **326**, 143 (2008).

[62] J. Noordmans, P. J. Wit, H. C. Van Der Mei, and H. J. Busscher, Detachment of polystyrene particles from collector surfaces by surface tension forces induced by air-bubble passage through a parallel plate flow chamber, J. Adhes. Sci. Technol. **11**, 957 (1997).

[63] N. Chatterjee, S. Lapin, and M. Flury, Capillary forces between sediment particles and an air–water interface, Environ. Sci. Technol. **46**, 4411 (2012).

[64] D.-H. Jeong, L. Xing, J.-B. Boutin, and A. Sauret, Particulate suspension coating of capillary tubes, Soft Matter **18**, 8124 (2022).

[65] R. Jäger, M. Mendoza, and H. J. Herrmann, Channelization in porous media driven by erosion and deposition, Phys. Rev. E **95**, 013110 (2017).

[66] S. Khodaparast, M. K. Kim, J. E. Silpe, and H. A. Stone, Bubble-driven detachment of bacteria from confined microgeometries, Environ. Sci. Technol. **51**, 1340 (2017).

[67] Y. E. Yu, S. Khodaparast, and H. A. Stone, Armoring confined bubbles in the flow of colloidal suspensions, Soft Matter **13**, 2857 (2017).

[68] A. D. Araújo, M. C. Romeu, A. A. Moreira, R. F. S. Andrade, and J. S. Andrade, Jr., Multiple-well invasion percolation, Phys. Rev. E **77**, 041410 (2008).

[69] See Supplemental Material at http://link.aps.org/supplemental/10.1103/PhysRevResearch.5.043015 for Movies S1–S9.

[70] L. Niemeyer, L. Pietronero, and H. J. Wiesmann, Fractal dimension of dielectric breakdown, Phys. Rev. Lett. **52**, 1033 (1984).

[71] A. Anbari, H.-T. Chien, S. S. Datta, W. Deng, D. A. Weitz, and J. Fan, Microfluidic model porous media: Fabrication and applications, Small **14**, 1703575 (2018).

[72] R. Lenormand, E. Touboul, and C. Zarcone, Numerical models and experiments on immiscible displacements in porous media, J. Fluid Mech. **189**, 165 (1988).

[73] P. Meakin, J. Feder, V. Frette, and T. Jøssang, Invasion percolation in a destabilizing gradient, Phys. Rev. A **46**, 3357 (1992).

[74] R. N. Onody, A. Posadas, and S. Crestana, Experimental studies of the fingering phenomena in two dimensions and simulation using a modified invasion percolation model, J. Appl. Phys. **78**, 2970 (1995).

[75] T. T. Al-Housseiny, P. A. Tsai, and H. A. Stone, Control of interfacial instabilities using flow geometry, Nat. Phys. **8**, 747 (2012).

[76] S. Jackson, H. Power, D. Giddings, and D. Stevens, The stability of immiscible viscous fingering in hele-shaw cells with spatially varying permeability, Comput. Methods Appl. Mech. Eng. **320**, 606 (2017).

[77] S. Biswas, P. Fantinel, O. Borgman, R. Holtzman, and L. Goehring, Drying and percolation in correlated porous media, Phys. Rev. Fluids **3**, 124307 (2018).

[78] N. B. Lu, C. A. Browne, D. B. Amchin, J. K. Nunes, and S. S. Datta, Controlling capillary fingering using pore size gradients in disordered media, Phys. Rev. Fluids **4**, 084303 (2019).

[79] N. B. Lu, A. A. Pahlavan, C. A. Browne, D. B. Amchin, H. A. Stone, and S. S. Datta, Forced imbibition in stratified porous media, Phys. Rev. Appl. **14**, 054009 (2020).

[80] N. B. Lu, D. B. Amchin, and S. S. Datta, Forced imbibition in stratified porous media: Fluid dynamics and breakthrough saturation, Phys. Rev. Fluids **6**, 114007 (2021).

[81] G. Jerauld and S. Salter, The effect of pore-structure on hysteresis in relative permeability and capillary pressure: Pore-level modeling, Transp. Porous Media **5**, 103 (1990).